ChemSusChem

Research Article
doi.org/10.1002/cssc.202401698

Chemistry Europe
European Chemical Societies Publishing

www.chemsuschem.org

A New Life for Tionite Industrial Waste: Regeneration Strategy towards Photocatalytic Applications

Lorenzo Viganò,[a] Barbara Di Credico,*[a] Francesco Parrino,*[b] Nicolas Keller,[c] Maurizio Bellotto,[d] Massimiliano D'Arienzo,[a] Silvia Mostoni,[a] Saverio Latorrata,[e] Anna Dotti,[e] Roberto Nisticò,[a] and Roberto Scotti[a]

Industrial waste management is an urgent problem to solve possibly by recycling, reuse and recovery of resources. In this framework, the sludge of the TiO_2 manufacturing, called tionite, is of certain interest because it contains metallic oxide-bearing impurities, dangerous to the environment. Hence, we propose a strategy to recover TiO_2 from tionite, towards its effective re-use as a photocatalyst. In detail, tionite was treated under acidic or alkaline conditions to remove impurities and improve the TiO_2 accessibility, and each single purification step was monitored by a thorough multi-technique characterization.

The photocatalytic activity of the modified tionite materials was tested for the partial oxidation of ferulic acid to vanillin, a relevant sustainable green reaction, being vanillin an industrially relevant high added value compound and ferulic acid an abundant component of lignin present in industrial waste. All the tionite catalysts have shown significant efficiency in terms of vanillin selectivity respect to the benchmark TiO_2 P25. In particular, the sample treated under acidic conditions showed the best performances, due to specific interaction between the organic substrates and the catalyst. Results demonstrated that an industrial waste such as tionite can be valorized by proposing a tailored regeneration strategy.

1. Introduction

The rapid depletion of natural resources and the increase in waste generation are critical issues for our society. Global natural resource consumption is forecast to rise 60% by 2060, compared with 2020 levels,[1] while municipal solid waste generation is predicted to grow from 2.3 billion tons in 2023 to 3.8 billion tons by 2050.[2] Therefore, one of the most pressing challenges of current materials research is not only trying to reuse exhausted materials or their components, but also valorizing industrial waste.[3] "The process of reusing, recycling or composting waste materials and converting them into more useful products including materials, chemicals, fuels or other sources of energy" is known as waste valorization[4] and can be obtained by i) processing of residues or by-products into raw materials, ii) using the discarded finished or semifinished products as raw materials or energy sources, or iii) adding waste materials in the manufacturing process steps.

In this context, the *sludge* generated as a waste of the titanium dioxide manufacturing process has become an urgent issue because it is usually disposed in landfills and contains metallic oxide-bearing impurities, potentially dangerous for the environment.[5] The concern is not negligible when considering that the worldwide production of titanium dioxide consists of millions of tons each year. In fact, titanium dioxide is a highly versatile semiconductor with photocatalytic properties,[6–8] widely used in coatings such as paints, plastics, papers, printing inks, pharmaceuticals, foodstuffs, and cosmetics.[9,10] In general, TiO_2 production relies upon chemical purification processes applied to suitable Ti containing minerals. The main processes are the chloride and sulfuric acid methods. The last one presents several advantages, being a mature and quite simple technology which uses abundant and easy to get raw materials. In detail, the feedstock is usually an ilmenite-based mineral ($FeTiO_3$) finely ground and dissolved in sulfuric acid in order to produce a mixture of titanyl ($TiOSO_4$) and ferric sulfates.[11,12] The liquor passes then to a clarification tank where the un-dissolved solids, i.e. the sludge, are allowed to settle and are separated from the solution by flocculation and filtration. Cooling the solution, by maintaining reducing environment, causes the precipitation of the ferric sulfate which is filtered off. The remaining titanyl sulphate solution gives rise first to hydrated titanium dioxide by reaction with water and then to pure TiO_2. The residue, finally neutralized and disposed, appears as a fine-

[a] *Department of Materials Science, INSTM, University of Milano-Bicocca, Milano, Italy*
[b] *Department of Industrial Engineering, University of Trento, Trento, Italy*
[c] *Institut de Chimie et Procédés pour l'Energie, l'Environnement et la Santé (ICPEES), CNRS/University of Strasbourg, Strasbourg, France*
[d] *Opigeo Srl, Padova, Italy*
[e] *Department of Chemistry, Materials and Chemical Engineering "Giulio Natta", Politecnico di Milano, Milan, Italy*

Correspondence: *Barbara Di Credico, Department of Materials Science, INSTM, University of Milano-Bicocca, Via R. Cozzi, 55, 20125 Milano, Italy.*
Email: barbara.dicredico@unimib.it

Francesco Parrino, Department of Industrial Engineering, University of Trento, Via Sommarive 9, 38123 Trento, Italy.
Email: francesco.parrino@unitn.it

Supporting Information for this article is available on the WWW under https://doi.org/10.1002/cssc.202401698

grained sludge and contains TiO_2 (rutile, anatase, amorphous phase), $CaSO_4{\cdot}0.5H_2O$ (bassanite), SiO_2, and Al, Ca, Mg, and Fe species in traces, as well as sulfur residuals. The composition of the sludge, known as tionite, poses crucial environmental problems, due to risks of contamination of both surface and underground water resources,[13] but at the same time entails promising features for specific applications. Surprisingly, the re-use of tionite has been only partially explored in literature. After the removal of the potential hazardous elements, tionite was successfully utilized as component in brickmaking or generally building materials,[14–16] and in fire-insulating materials.[17] Also the recovery of titanium dioxide from tionite has been investigated, by removing silicon though a complex process involving hydrothermal conversion, water washing, and acid leaching.[5] However, the recovery efficiency of this process has not been evaluated, thus discouraging real applications. Recently, the possible use of tionite as a photocatalyst was considered by embedding it into a reduced graphene oxide membrane.[18] The experimental results highlighted the limited contribution of the tionite to the photocatalytic efficiency, suggesting that a critical purification treatment would be mandatory to exploit the catalytic properties of the titanium dioxide component inside the industrial sludge.

In this context, the present study aims at developing a regeneration strategy of tionite with the final goal to obtain a photocatalytic active material. Step by step, we designed specific chemical treatments to improve the catalytic performance and provide a new life for the tionite waste. The treatments were established to remove impurities and improve the titanium dioxide accessibility in a simple way, by using acid and basic aqueous solutions. Each single purification step was monitored by a careful multi-technique characterization, based on chemical, structural and morphological analysis. Preliminary photocatalytic tests of paracetamol (PC) degradation showed a modest photocatalytic activity for applications in the traditional field of environmental remediation. Therefore, we investigated the possibility to use this material for selective partial oxidation reactions, which generally require photocatalysts with low oxidizing power, but enabling specific surface interactions with the organic substrates. For instance, poorly crystallized (and poorly active) TiO_2 samples are reported to trigger the photocatalytic partial oxidation of alcohols to aldehydes with outstanding selectivity values.[5] Inspired by these results, in the present work we investigated the possibility of obtaining selectively vanillin from ferulic acid in the presence of tionite. This reaction is particularly relevant in terms of sustainable production. In fact, ferulic acid is one of the main components of lignin and it represents a waste compound in many aqueous effluents downstream of several agro-food processes. However, it can be used as starting material for the synthesis of high-added value compounds such as vanillin in view of circular economy applications.[19,20] In fact, vanillin is probably the most relevant flavor compound and its industrial green production is currently performed with low selectivity values.[21] The present study shows, as a proof of concept, that it is possible to take advantage of the peculiar features of a waste material and to propose regeneration strategies enabling applications in specific and tailored fields. In other words, sustainability can be efficiently implemented only by carefully matching the requirements of specific applications with fundamental knowledge of the properties of the waste/resource.

2. Experimental

2.1. Materials

Paracetamol (PC) 98% was purchased from Thermo Scientific and used as received. Sodium hydroxide $\geq$98% and H_2O HPLC grade were purchased from VWR. Hydrofluoric acid 38–40%, acetonitrile HPLC grade $\geq$99.9%, glacial acetic acid $\geq$99%, vanillin $\geq$99%, and ferulic acid $\geq$99% were purchased from Sigma-Aldrich. Milli-Q water with a resistivity $\rho > 18.2\ M\Omega{\cdot}cm$ was used.

An undissolved residue known as "tionite", hereby labelled as St-Tionite (starting tionite), was generated during the digestion of titanium-rich minerals in the sulfate process of TiO_2 production[22] performed by the Venator TiO_2 plant in Scarlino (Italy). Tionite was provided in two forms, either lime neutralized which is the usual industrial processing route to prepare the material for landfilling, or as a raw acidic material. The raw acidic tionite was neutralized with NaOH to pH = 7, by adding NaOH 0.77 M dropwise to a slurry of tionite 1:5 by weight in water. The neutralized slurry was then washed, filtered and dried. The two forms of tionite are labelled as nCa_Tionite and nNa_Tionite respectively and were then used as such or treated as described below.

2.2. Acid and Basic Treatments of nNa_Tionite

The acid treatment of nNa_Tionite was carried out by dispersing 200 mg of the powder in 50 ml of a 5% HF aqueous solution, at room temperature (RT) and under magnetic stirring for 24 h. The precipitate was separated by centrifugation at 9000 rpm for 10 min, washed three times with dH_2O, and finally dried overnight at 80 °C. The sample was labelled "nNa_Tionite_A".

The basic treatment of nNa_Tionite was carried out by dispersing 200 mg of nNa_Tionite in 50 ml of NaOH 1 M aqueous solution at 100 °C under magnetic stirring for 24 h. The suspension was then centrifuged at 9000 revolutions per minute (rpm) for 10 min and the solid residue was washed with NaOH 1 M and then three times with distilled H_2O (dH_2O), followed by centrifugation. At the end, the sample was dried overnight at 80 °C. The sample was labelled "nNa_Tionite_B".

Scheme 1 summarizes the treatments and samples described above.

2.3. Characterization of the Tionite-Based Materials

Fourier-transformed infrared (FTIR) spectra were collected with an attenuated total reflectance (ATR) setup on a ThermoFisher

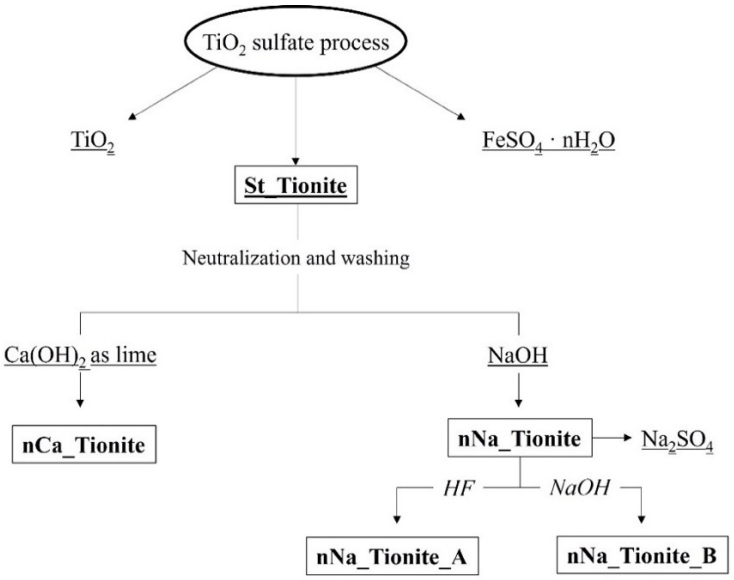

Scheme 1. Flow sheet of the recovering process of St-Tionite with the chemical treatments applied.

Nicolet iS20, in the range 4000–550 cm^{-1} with a spectral resolution of 4 cm^{-1} and 128 scans.

Thermogravimetric analysis (TGA) was performed by using a Mettler Toledo TGA/DSC1 STARe System at a constant air flux (50 cm^3 min^{-1}). The sample weight loss was measured in the range 30–1000 °C at the heating rate 10 °C min^{-1}, with an isotherm at 150 °C for 15 min, to remove humidity, and at 1000 °C for 5 min.

In addition, TGA coupled to FTIR (TGA/FTIR) analysis was performed by coupling the instruments described above using the above reported specifics.

Powder X-ray diffraction (XRD) patterns were obtained by means of a Rigaku MiniFlex 600 diffractometer with 0.154 nm Cu Kα radiation in the 2θ range of 5–90°, 2θ step 0.02°, scan rate 1° min^{-1}.

Elemental analysis (CHNS) was carried out by using Elemental VarioMICRO analyzer, setting the temperature of the combustion and reduction columns at 1150 °C and 850 °C respectively. The results reported are the average and standard deviation of three measurements.

Tionite-based materials were morphologically characterized by Scanning electron microscopy (SEM) and Transmission electron microscopy (TEM) analyses. SEM images were collected with a Zeiss Gemini 500 microscope in a high-vacuum configuration equipped with a Bruker Quantax detector for Energy Dispersive microanalysis (EDX). The electron beam excitation was 30 kV at a beam current of 25 pA, and the working distance was 12 mm. In this configuration, the beam spot was 38 nm. The samples were dispersed in EtOH, deposited onto an aluminum substrate by drop-casting and sputtered with gold. SEM-EDX maps were all acquired with a 1000x magnification. TEM micrographs were collected with a JEOL JEM-2100Plus transmission electron microscopy, operating at an acceleration voltage of 200 kV and equipped with an 8-megapixel Gatan Rio complementary metal-oxide-semiconductor camera. Samples were dispersed in ethanol and deposited on carbon-coated Cu TEM mesh grids by drop-casting.

X-ray Fluorescence Spectroscopy (XRF) was performed by using a micro-XRF spectrometer (Bruker ARTAX 200) equipped with a Mo anode X-ray tube, collimated down to 0.65 mm in diameter (excited sample area of 0.33 mm^2). The working conditions were 20 kV and 1.0 mA with an acquisition time of 300 s. Spectra were normalized on the Ti peak.

Raman spectra were obtained with a Jasco Ventuno μ-Raman instrument with a Peltier-cooled charge-coupled device (CCD) camera (operating temperature: - 50 °C) and a He–Ne laser (wavelength, 632.8 nm; power density, 6 $kWcm^{-2}$).

N_2 physisorption isotherms on tionite samples were recorded at 77 K in a liquid N_2 bath by a Micromeritics ASAP 2420 apparatus. Prior to analysis, all materials were degassed for 3 h at 100 °C under vacuum. The specific surface area (SSA) was calculated according to the Brunauer–Emmett– Teller (BET) method,[23] using adsorption data in the 0.07 – 0.25 relative pressure range. Pore size distributions were determined through the Barrett-Joyner-Halenda (BJH) method with Harkins-Jura curve between 2 and 100 nm. Pore volumes were estimated from the volume of N_2 adsorbed at $P/P^0 = 0.99$.

The contact angle analysis was performed using an in-house contact angle setup, consisting of a camera (Fastcam Nova S6, Photron) with Tokina AT–X PRO D (100 mm F2.8 MACRO) as optical lens and backlight illumination. The static contact angle was measured with a drop volume of 6 μl. The data reported are the average and standard deviation of three measurements.

2.4. Photocatalytic Tests Procedure

The photocatalytic experiments with PC were performed in a 0.5 L cylindrical Pyrex batch photoreactor. A 125 W medium-pressure Hg lamp (Helios Italquartz, Italy), with a maximum

emission at about 365 nm, was axially immersed within the photoreactor. The suspension was kept in the dark for 30 min to reach the adsorption-desorption equilibrium, with O_2 bubbling at a flow rate of 50 ml min^{-1}. The solution temperature during the experiment was controlled by the circulation of water through a jacket surrounding the reactor. A magnetic stirrer was used to guarantee the homogeneity of the reaction mixture. The catalyst amount was 0.4 g L^{-1}, and the initial PC concentration was 30 mg L^{-1}. Samples were withdrawn at fixed times; the supernatant was filtered through a 0.22 μm hydrophilic PTFE syringe filter (VWR). The quantitative determination of PC was performed with an HPLC Agilent 1100 series equipped with a ZORBAX Eclipse XBD–C18, 5 μm, 150 x 4.6 mm column and a UV-Vis detector set at 243 nm. The eluent, consisting of 90% v/v of water and 10% v/v acetonitrile, had a flow rate of 0.8 ml min^{-1} and the injection volume was 20 μL.

Photocatalytic runs have been performed in triplicate and standard deviation was within ± 5%.

Photocatalytic partial oxidation of ferulic acid to vanillin was performed in a cylindrical Pyrex reactor (internal diameter 3 cm) containing 30 mg of the photocatalyst dispersed in 50 mL of a 0.5 mM ferulic acid aqueous solution. The mixture was sonicated for 5 min at RT and stirred for 30 min under dark conditions. The obtained suspension was irradiated by UV–A light under a constant O_2 flux by means of six actinic lamps (15 W each, $\lambda_{max} = 365$ nm, total radiant flux 40.15 W m^{-2}) hexagonally arranged at the same distance from the reactor placed in the center. The photonic flux impinging the photocatalytic suspension was measured by using a Delta Ohm photo quantum meter (model HD9021, Selvazzano Dentro, Italy) equipped with a LP 9021 UVA sensor probe. The amount of photocatalyst dispersed corresponded to reaction conditions at which the photonic flux exiting from the reaction medium was *ca.* 10% of the impinging one. This ensures a safe comparison of the results obtained in the presence of different photocatalysts. Samples of the reaction mixture were withdrawn at fixed times and filtered (hydrophilic PTFE syringe filter, 0.22 μm, VWR). Selected photocatalytic runs have been performed in triplicate and standard deviation was within ± 5%.

The ferulic acid photo-adsorption behavior of all samples was investigated by performing photocatalytic runs under the same experimental conditions described above, but under N_2 flux before and during the irradiation to remove O_2 and avoid ferulic acid degradation.

The quantitative determination of ferulic acid and vanillin was performed with a Shimadzu HPLC Prominence equipped with a Shimpack GWS C18, 5 μm, 150 x 4.6 mm column and a diode-array UV-vis detector. The HPLC chromatograms were obtained at 322 nm, with a flow rate of 0.7 mL min^{-1}, and an injection volume of 20 μL. The eluent consisted of a solution containing 80% v/v of a 1% v/v CH_3COOH aqueous solution and 20% v/v acetonitrile.

The vanillin selectivity values were calculated during irradiation according to Eq. 1:

$$S\%\ [\text{Vanillin}]t = \frac{[\text{Vanillin}]_t}{\Delta[\text{Ferulic acid}]} \cdot 100 \quad (1)$$

where [Vanillin]t is the vanillin concentration at the sampling time t and Δ[Ferulic acid] is the variation of the ferulic acid concentration between the sampling time t and the initial concentration (t = 0 min).

2.5. Adsorption Test Procedure

nNa_Tionite and nNa_Tionite_B samples were tested for the adsorption of vanillin and ferulic acid. Four different concentrations were used for both molecules (0.25, 0.1, 0.05 and 0.01 mM) in the presence of a constant amount of photocatalyst. The amount of sample used was calculated to keep constant the amount of the TiO_2 component in the two tests. EDX analysis revealed a 45% content of TiO_2 for the nNa_Tionite sample, while the amount of TiO_2 in the nNa_Tionite_B sample was calculated by considering the mass lost during the chemical treatment. The suspensions were left under magnetic stirring overnight to reach the adsorption-desorption equilibrium and then the photocatalyst was separated by filtration (hydrophilic PTFE syringe filter, 0.22 μm, VWR). The quantification of vanillin and ferulic acid in the solution was carried out by HPLC, as described above. The experimental data were fitted by using the Langmuir isotherm model (Eq. 2:[24]

$$Q_e = \frac{q_0 K C_e}{K C_e + 1} \quad (2)$$

where Q_e is the amount of vanillin adsorbed at the equilibrium, q_0 is the maximum amount of vanillin adsorbed per adsorbent mass, C_e is the vanillin concentration in solution at the equilibrium, and K is the thermodynamic adsorption constant.

3. Results and Discussion

3.1. Structural and Morphological Characterization of Pristine nCa_Tionite and nNa_Tionite

To re-use and recycle the titanium dioxide-based waste material for photocatalytic applications, a thorough characterisation of the as-received neutralised tionite samples was carried out (Figure 1), thus implementing the datasheet information on the elemental composition provided by the company.

XRF analysis of the nCa_Tionite sample (black spectrum in Figure 1a) shows that the main components are Ti, Fe and Ca species, represented by both Kα1 and Kβ1 signals. Peaks with lower intensity can be related to the presence of Si, S, K and Mn (inset in Figure 1a). TiO_2 is the most abundant component of the material, accounting for almost 30% of the sample. In addition, nCa_Tionite contains a non-negligible amount of Si (16% as SiO_2) and Ca (12.7% as CaO), with small traces of Fe, Al and Mn (2.48% as Fe_2O_3, 2.99% as Al_2O_3 and 0.34% as MnO).

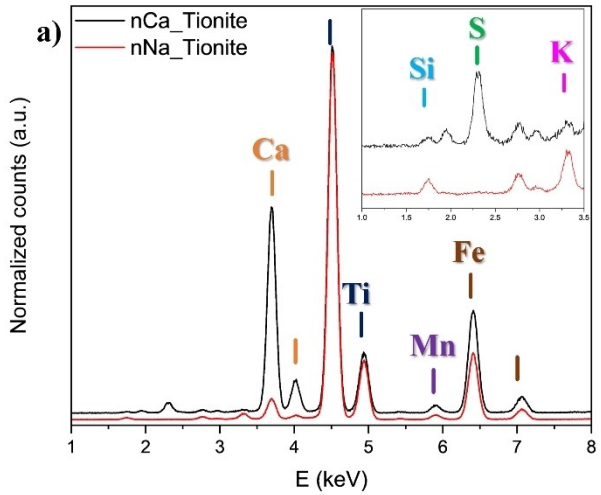

b)

	nCa_Tionite	nNa_Tionite
C (%)	4.37 (±0.53)	5.0 (±0.3)
H (%)	1.5 (±0.17)	1.10 (±0.04)
N (%)	0.18 (±0.12)	0.27 (±0.05)
S (%)	4.54 (±0.55)	0.28 (±0.05)

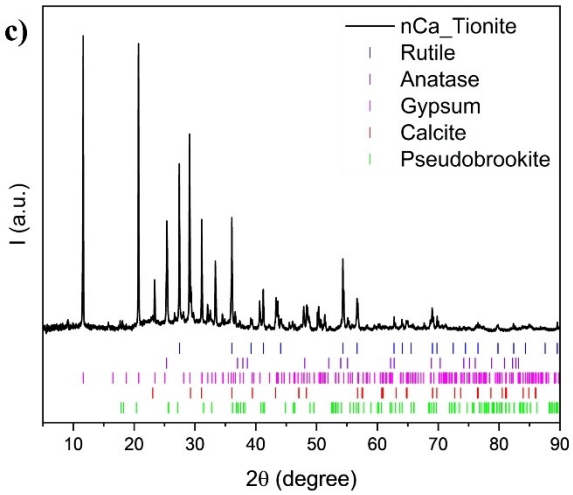

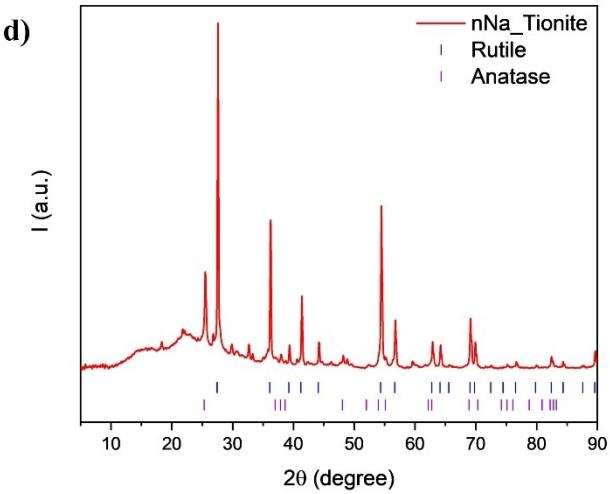

Figure 1. a) XRF spectra with the magnification of the range 1–3.5 keV in the inset; b) CHNS results and c,d) XRD spectra of nCa_Tionite (black) and nNa_Tionite (red). Reference diffractograms of rutile (blue), anatase (purple), gypsum (pink), calcite (red) and pseudobrookite (green) are reported.

The non-metallic components of nCa_Tionite were quantified by the CHNS elemental analysis. The results, in Figure 1b, show that nitrogen is virtually absent, while considerable weight percentages of carbon and sulfur species were detected.

In order to understand how these elements are combined in nCa_Tionite, XRD analysis was performed. The XRD pattern (Figure 1c) shows a large number of peaks, indicating the presence of several crystalline phases: the main phases are TiO_2 in both anatase and rutile form, gypsum ($CaSO_4{\cdot}2H_2O$), calcite ($CaCO_3$) pseudobrookite ($FeTiO_3$) and an amorphous phase. A crucial aspect for the photocatalytic application relies on the rutile content in the sample compared to the anatase one, and the nCa_Tionite sample exhibits a very high rutile/anatase ratio of 82:18.

Using NaOH, instead of $Ca(OH)_2$ for the neutralization of St_Tionite, allowed to simplify the composition of nNa_Tionite with respect to nCa_Tionite, thanks to the elimination of the sulfate anions in the form of water soluble Na_2SO_4, by avoiding the formation of $CaSO_4{\cdot}2H_2O$. In fact, the XRF spectrum of nNa_Tionite (red spectrum in Figure 1a) indicates a composition similar to nCa_Tionite, with a net decrease of the Ca content and the disappearance of the sulfur signal at 2.31 keV. The absence of $CaSO_4$ is also confirmed by CHNS analysis (Figure 1b) as the sulfur weight % is virtually null, especially when compared to nCa_Tionite. Accordingly, the patterns related to both calcite and gypsum are absent in the nNa_Tionite diffractogram (Figure 1d). Moreover, the rutile/anatase weight ratio (86:14) did not change significantly with respect to nCa_Tionite. It is worth noticing that the XRD diffractograms of both nCa_Tionite and nNa_Tionite samples show a broad halo in the 2θ range between 20 and 40° that can be ascribed to the presence of amorphous phases. The carbonaceous nature of this phase can be inferred, by considering that the amount of carbon in the two samples is similar (Figure 1b), even though the calcite component is absent in the nNa_Tionite one. Moreover, the contribution of an amorphous siliceous component is also probable (as confirmed by XRD after further treatments, as reported below in Paragraph 3.2).

The Raman spectrum of nCa_Tionite (black line in Figure 2a) corroborates the XRD results. Indeed, the signals attributed to both anatase and rutile TiO_2 phases,[25] calcite,[26] and gypsum[27]

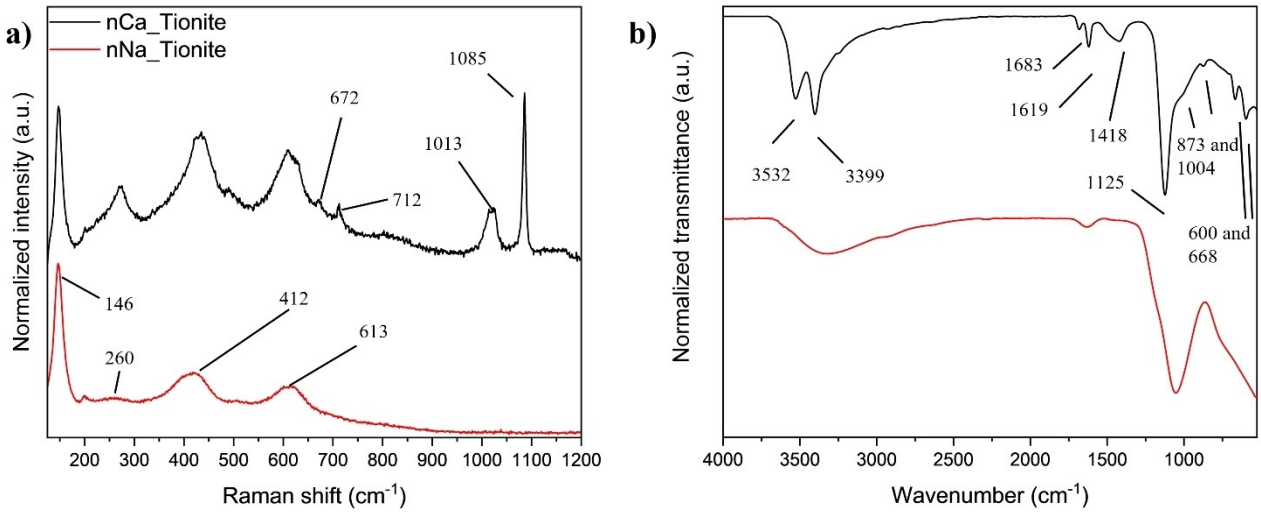

Figure 2. a) Raman and b) ATR-FTIR spectra of nCa_Tionite (black) and nNa_Tionite (red).

could be detected (attributions reported in Table S1 of Supporting Information, SI).

The IR spectrum of the nCa_Tionite sample (black line in Figure 2b) confirms the presence of the $CaSO_4$ gypsum phase.[28] In fact, the bands of OH stretching and bending, at 3532, 3399 cm^{-1} and at 1619, 1683 cm^{-1}, respectively, in combination with the signal at 668 and 600 cm^{-1}, attributed to sulphate bending, can be observed. Moreover, the signals at 1125 and 1004 cm^{-1} confirm the presence of silica or silicate, supporting the composition analysis results. The signals at 709, 872 and 1418 cm^{-1} can be attributed to different CO_3^{2-} stretching vibrations of calcite.[29] Finally, the band in the region between 900 and 500 cm^{-1} is associable with several metal-O signals, including Ti–O stretching.[30] More details on attributions are listed in Table S2.

TGA analysis provides information on thermal phenomena of nCa_Tionite (black line, Figure S1a). Part of the weight loss up to 150 °C could be related to adsorbed water molecules and gypsum dehydration steps: at a temperature above 95 °C bassanite ($CaSO_4 \cdot 0.5\ H_2O$) is the more stable phase, whereas above 120 °C anhydrite is obtained ($CaSO_4$).[31] The weight loss between 650 and 750 °C can be associated to the calcite decomposition to CaO.[32] The attribution of the thermal phenomena occurring between 300 and 400 °C is not straightforward, due to the lack of exhaustive comprehension of the material composition. However, coupling TGA with FTIR spectroscopy (results shown in Figure S1b) revealed that the most relevant signal detected between 300 and 400 °C corresponds to CO_2 release, which could tentatively derive from the thermal decomposition of the amorphous carbon phase detected by elemental analysis (Figure 1b).

From the morphological point of view, the SEM images (Figure S2) of nCa_Tionite show a complex material with no defined or uniform morphology, even if the characteristic rod-shaped crystals (red arrows in figure)[33] confirm the presence of gypsum. In addition, TEM micrographs evidence the different morphology of nCa_Tionite with nanometric aggregated particles (Figure 3) and bigger lamellar structures showing small particles distributed on their surface.

The Raman spectrum of the nNa_Tionite sample (Figure 2a) shows the main signals of rutile and anatase TiO_2, while the signals above 650 cm^{-1} detected for nCa_Tionite and attributed to the two inorganic species containing Ca (gypsum and calcite) are absent, as described above.

The ATR-FTIR spectrum of nNa_Tionite (Figure 2b) exhibits some of the bands already observed for nCa_Tionite: specifically, the band between 500 and 800 cm^{-1} attributed to metal-O bonds stretching, including Ti–O bond, and the signal at 1057 cm^{-1} due to Si–O–Si bond stretching. However, the

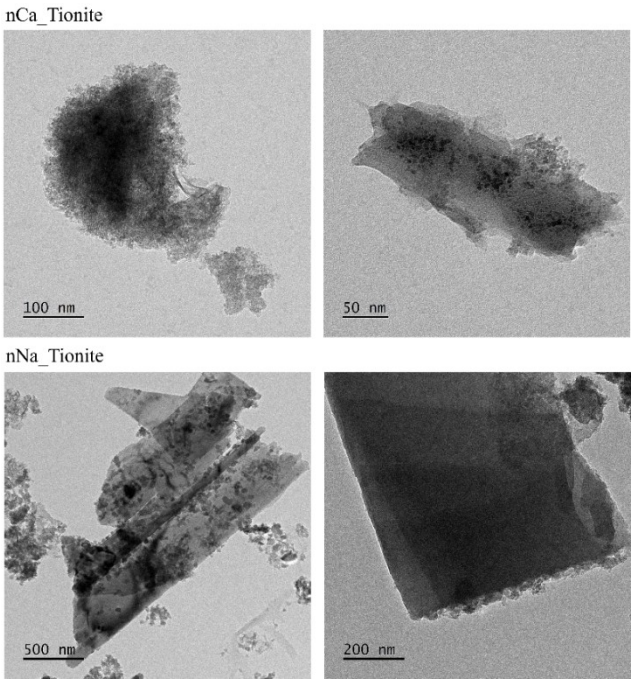

Figure 3. TEM micrographs of nCa_Tionite and nNa_Tionite.

spectrum did not show the signals attributed to inorganic sulfate and carbonate, further confirming the efficiency of the new neutralization process.

nNa_Tionite thermogram exhibits only one major weight loss between 250 and 450 °C, associated to CO_2 loss (Figure S1a,b), which was also observed for nCa_Tionite. The water release at temperature below 150 °C is of lower extent with respect to the nCa_Tionite sample. On the other hand, the weight loss between 650 and 750 °C, observed for nCa_Tionite, is absent, further confirming the absence of calcite in the sample.

SEM images (Figure S2) suggest that nNa_Tionite consists of particles of different morphologies with inhomogeneous dimensions, ranging from fraction of μm to more than 10 μm. Notably, particles with a bidimensional sheet-like shape can be observed, as confirmed by TEM micrographs (Figure 3), showing nNa_Tionite as aggregated nanometric particles and sheets-structured elements decorated by smaller nanoparticles.

SEM analysis with EDX mapping was performed in order to highlight the elemental distribution within both nCa_Tionite and nNa_Tionite samples (Figure 4).

In the nCa_Tionite sample, Ti forms isolated TiO_2 structures uniformly distributed, while Mg, Si and Al species are distributed randomly and their colocalization suggests the presence of Mg-rich aluminosilicates. The presence and colocalization of Ca and S (Figure S3), confirm the presence of $CaSO_4$ in the materials. Figure S3 also shows that iron is randomly distributed.

Also in the nNa_Tionite sample, titanium is distributed uniformly; however the silicon amount in the sample is remarkable when compared with the nCa_Tionite sample. Notably, Si atoms are co-localized on sheet-like particles with Al, Mg, Na, K, and Ca species present in lower quantities (Figure S3), suggesting that the bidimensional elements of nNa_Tionite are essentially aluminosilicate with Na, Mg, K and Ca acting as counterions. Finally, iron species are low in extent and inhomogeneously distributed in the nNa_Tionite sample, whereas sulfur is absent.

3.2. Structural and Morphological Characterization of Modified nNa_Tionite_A and nNa_Tionite_B

Further purification steps were carried out only on the nNa_Tionite sample, due to its simpler chemical composition compared to the nCa_Tionite one. To further enhance the relative amount and the accessibility of the titanium dioxide component for photocatalytic applications, a basic and an acidic treatment were performed in order to remove the photocatalytically inert aluminosilicate counterpart and the

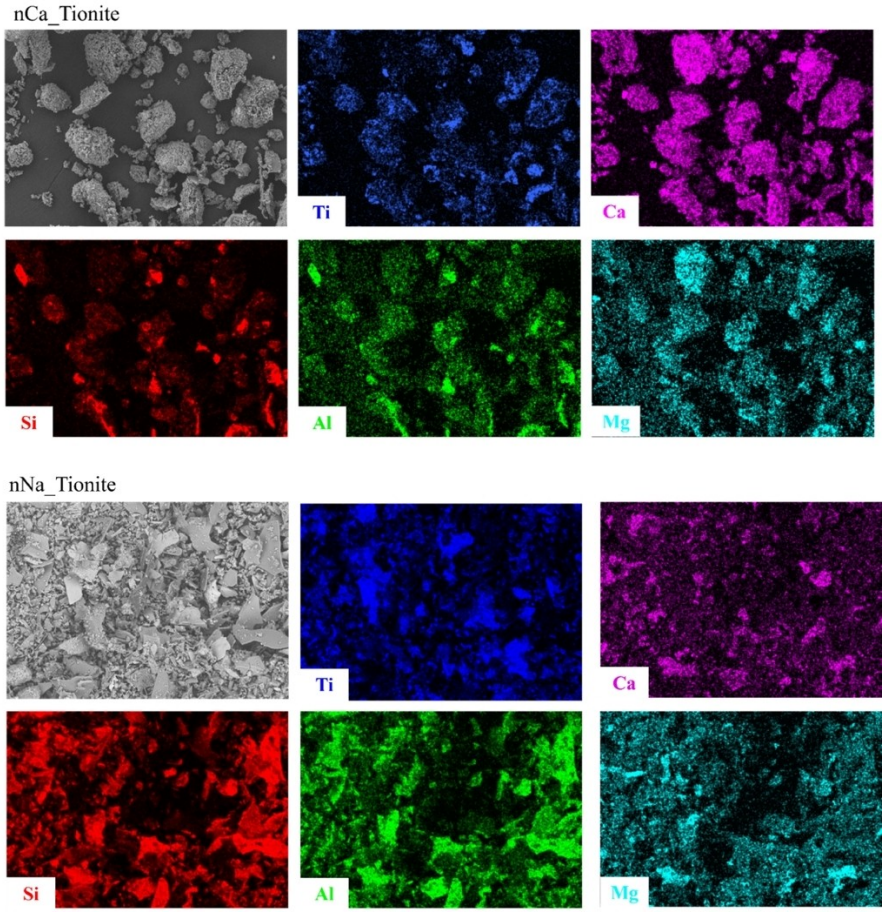

Figure 4. SEM images with the associated EDX mapping analysis of nCa_Tionite and nNa_Tionite.

traces of metal ions, which could act as recombination centres for the photogenerated charges, thus possibly reducing the photocatalytic activity.

The changes in the composition of nNa_Tionite after the treatment with NaOH (nNa_Tionite_B) can be highlighted by means of XRF and ATR-FTIR spectroscopies, as reported in Figure 5. The XRF spectra (Figure 5a) show that the basic treatment only slightly reduced the intensity of the iron signals, while, more interestingly, it completely removed the K and Si signals. These results are also confirmed by ATR-FTIR spectroscopy (Figure 5b) as the spectrum of nNa_Tionite_B shows the dramatic reduction of the Si–O–Si bond stretching band at 1057 cm^{-1}, also supported from the decrease of the amorphous phase in the XRD spectrum (Figure S4).

Similar results were obtained after the acidic treatment. In fact, the XRF and FTIR (Figure 6) and XRD (Figure S4) spectra confirm the complete removal of the silicate component from the sample, even if with a more remarkable decrease in the concentration of Fe, Ca and Mn, compared to nNa_Tionite_B.

To further assess the variation in composition taking place upon acidic and basic treatment, SEM-EDX analysis was performed (Figure 7). SEM micrographs show that the basic treatment only slightly affects the morphology of the sample, while the acidic treatment produces major changes in terms of particles size and shape. The net decrease in the amount of both Si and Al, as indicated by XRF and FTIR analysis for both samples, is therefore evident from the EDX images of the nNa_Tionite_B sample, while it could be masked by the morphological changes in the nNa_Tionite_A sample.

Similar conclusions can be drawn for other elements, like Mg, Ca and Fe (Figure S5).

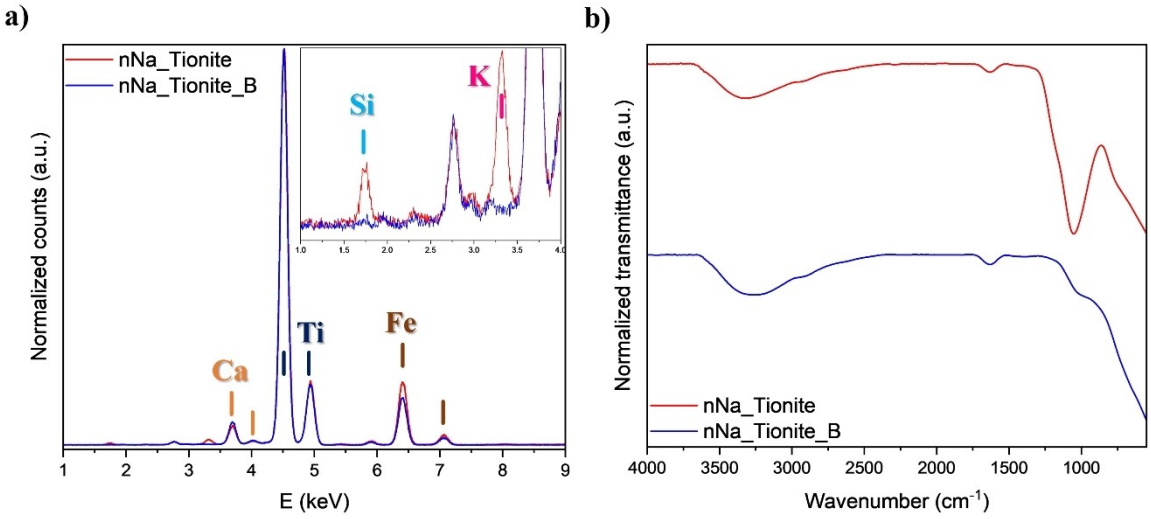

Figure 5. a) XRF and b) ATR-FTIR spectra of nNa_Tionite_B (blue) in comparison with nNa_Tionite (red).

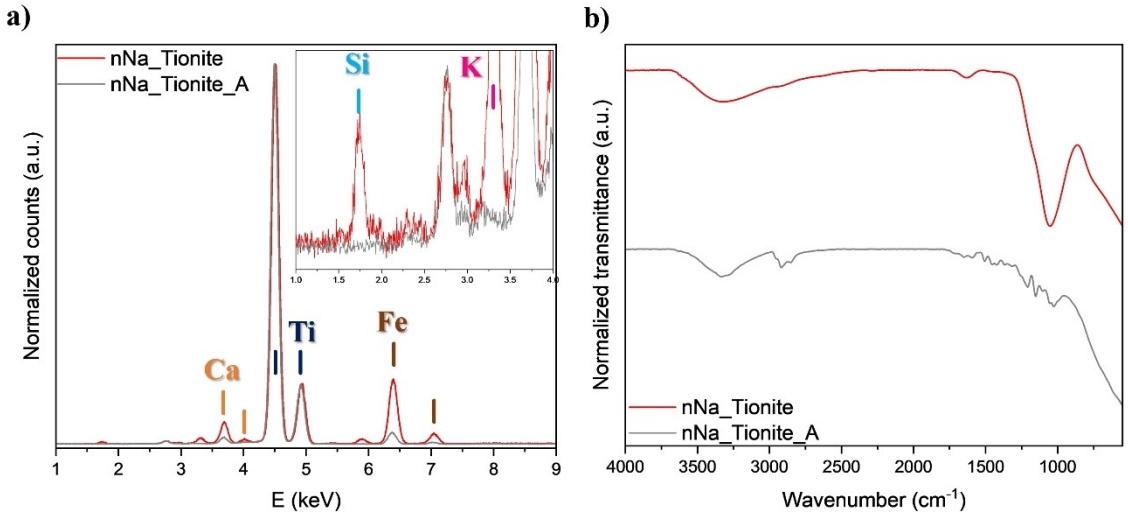

Figure 6. a) XRF and b) ATR-FTIR spectra of nNa_Tionite_A (grey) in comparison with nNa_Tionite (red).

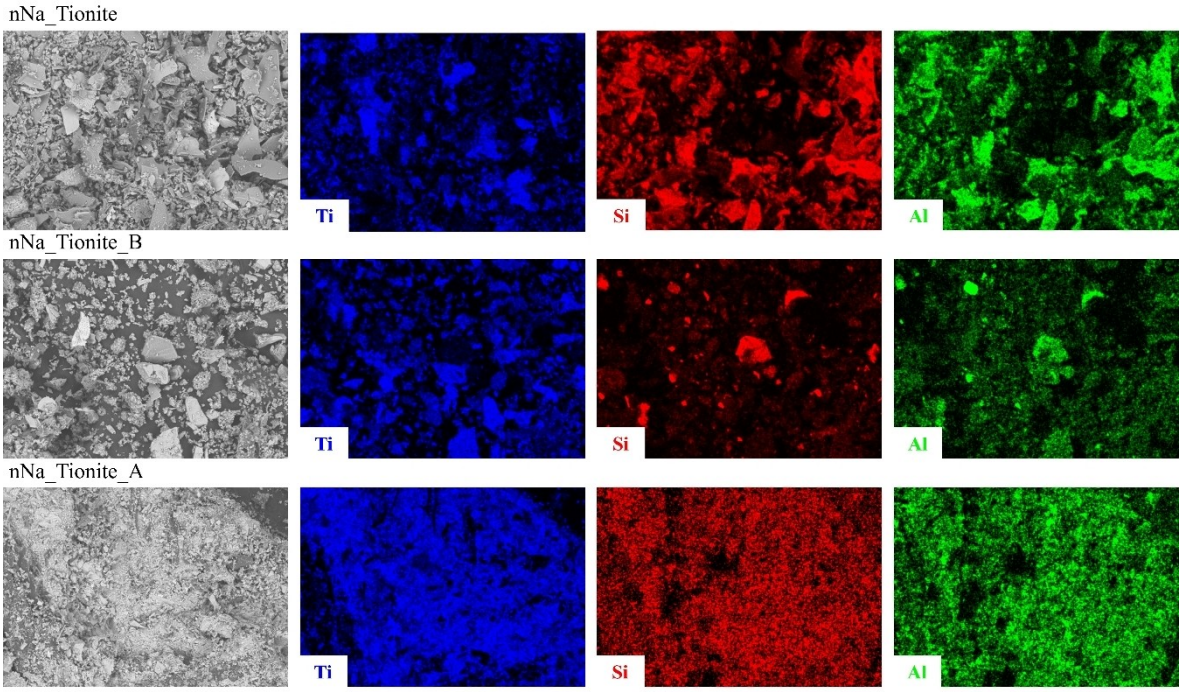

Figure 7. SEM images with the associated EDX mapping analysis of nNa_Tionite and nNa_Tionite_B in comparison to nNa_Tionite_A.

3.3. Surface Characterization of Pristine and Modified Tionite Materials

Contact angle measurements were performed to highlight the surface hydrophilicity of the samples, which can be roughly correlated with the surface hydroxylation degree. The pictures recorded during the sessile drop procedure are reported in Figure S6a, while the contact angle values are listed in Figure 8a, along with the SSA and the pore volume values. Both nCa_Tionite and nNa_Tionite samples show a contact angle value lower than 90°, indicating their hydrophilicity. In detail, the presence of gypsum and calcite in nCa_Tionite could be responsible for the relatively higher contact angle value. The basic treatment with NaOH does not significantly alter the surface properties of the nNa_Tionite material, as the contact angle of the nNa_Tionite_B only slightly increased. Contrarily, the HF treatment leads to a net increase in the contact angle, indicating a less hydrophilic surface. This result is in agreement with the relevant literature on the fluorination of metal oxides such as TiO_2,[34–37] which is reported to confer surface hydrophobicity. In fact, the surface of TiO_2 is reported to undergo a ligand exchange of the hydroxyl with the fluoride groups, promoted by their similar ionic radius. The efficiency of this displacement is strongly dependent on both the pH and fluoride concentration in the solution. In particular, the process is favored under acidic pH (approximatively 3) and at high fluoride concentrations. Since the acidic treatment is carried out by using a 5% HF aqueous solution, both conditions are fulfilled. To confirm the surface fluorination of nNa_Tionite_A, SEM-EDX mapping was performed (Figure S6b), highlighting a significant amount of fluorine in the sample, while the same element was completely absent in the other tionite samples.

N_2 isotherm adsorption analysis was performed on each sample to quantify SSA and porosity. The isotherms of all samples (in Figure 8b) can be ascribed to type IV, according to the IUPAC classification,[38] which is typical for mesoporous materials. The hysteresis can be categorized as H3, which indicates the presence of slit-shaped pores. Notably, the nNa_Tionite_B sample shows a significant hysteresis, with a step in the desorption branch between 0.4 and 0.5 P/P^0, with a higher surface area and pore volume respect the others.[39] From the values listed in Figure 7a, it is apparent that performing the neutralization step with $Ca(OH)_2$ produces a sample with slightly lower SSA value (56 m^2/g) compared to the NaOH process (68 m^2/g). Moreover, the subsequent basic treatment of the nNa_Tionite sample produces a relatively low increase of the surface area (from 68 to 85 m^2/g), possibly due to the dissolution of the aluminosilicate component. Contrarily, the HF treatment caused a strong reduction of the SSA of the nNa_Tionite_A sample (*ca.* 7 m^2g^{-1}, below the instrumental limit). These observations are in good agreement with the porosity results reported in Figure 8a–c. The nNa_Tionite sample shows higher mesoporosity than the nCa_Tionite one, in agreement with the higher surface area. The subsequent basic treatment of nNa_Tionite sample strongly increases the mesoporosity, possibly due to the opening of new pores or the exposure of already existing ones, which were closed by silica-like phases. On the contrary, the reduced SSA of the nNa_Tionite_A sample is well reflected in the low porosity of the sample. Considering the higher dissolving efficiency of HF, the structure might be corroded to the point of losing porosity to a certain extent, or

a)

	Contact angle (°)	SSA (m^2/g)	V pore (cm^3/g)
nCa_Tionite	49 (± 2)	56	0.142
nNa_Tionite	< 20	67	0.112
nNa_Tionite_B	31 (± 4)	85	0.155
nNa_Tionite_A	94 (± 5)	7	0.0386

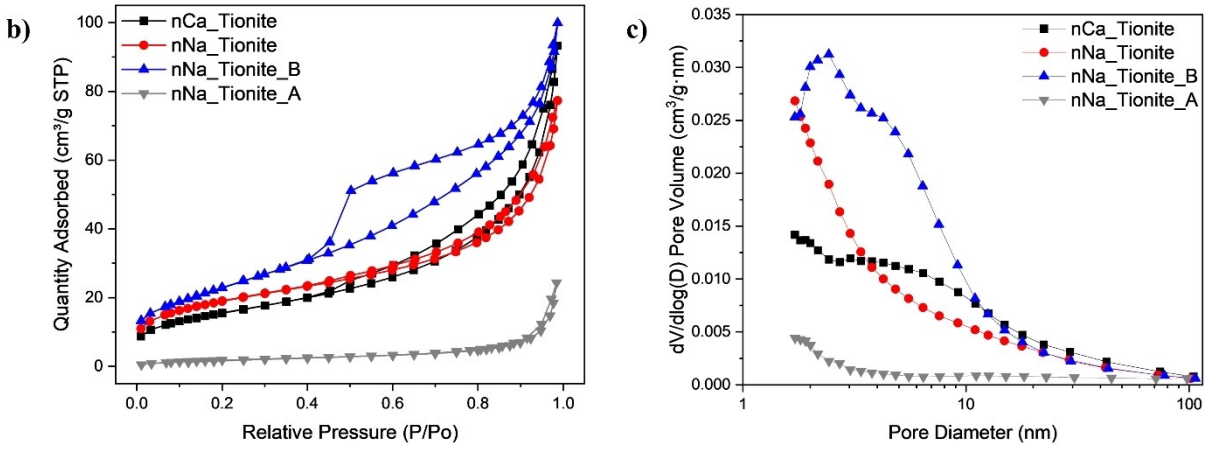

Figure 8. a) Table with contact angle, SSA and pore volume values, b) N_2 adsorption-desorption isotherms at 77 K and c) pore size distribution curves by BJH method for nCa_Tionite (black), nNa_Tionite (red), nNa_Tionite_B (blue) and nNa_Tionite_A (grey).

alternatively, the fluorine surface substitution could block or narrow mesopores as elsewhere reported.[40,41]

3.4. Photocatalytic Activity of Tionite-Based Materials

Pristine and treated tionite materials were initially tested for the degradation of PC in water to get, information on the viability of the tionite purification strategy and at the same time to check the feasibility of environmental applications. In fact, PC is a widely used antipyretic and analgesic drug, which is excreted unchanged or after being transformed in toxic metabolites. In this way, it reaches natural aqueous effluents where it enters the food chain and affects the growth and reproduction of aquatic organisms, especially upon long term exposure.[42] Robust and cheap TiO_2-based photocatalysts efficiently mineralize PC even under simulated solar light irradiation.[43]

However, as shown in Figure 9, the preliminary results on both nCa_Tionite and nNa_Tionite samples showed poor photocatalytic activity under UVA irradiation, maybe related to the low accessibility of light and/or reactant for titanium dioxide, which led to subsequent acid and basic treatments. Unfortunately, even if better efficiency was obtained, the most active sample (nNa_Tionite_A) provided only 43 % degradation of PC after 6 h irradiation, while the figures obtained in the presence of the other samples ranged between 17 and 28 %.

Notably, even the addition of nearly stoichiometric amounts of H_2O_2 did not significantly improve the photocatalytic activity (data not shown). The rather low oxidizing power of tionite discouraged us from proposing traditional environmental applications for this waste material. Instead, this feature could be remarkably useful in the field of photocatalytic partial oxidations, where the formation of high added value intermediate compounds could be maximized in the presence of suitable photocatalysts, which limit the overoxidation of the desired products. Therefore, the partial oxidation of ferulic acid to vanillin (Scheme 2) was studied using tionite as the photocatalyst.

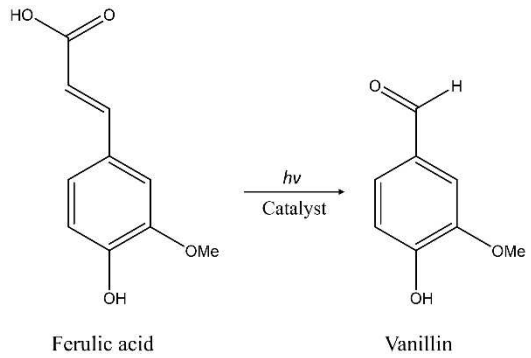

Scheme 2. Ferulic acid partial oxidation to vanillin.

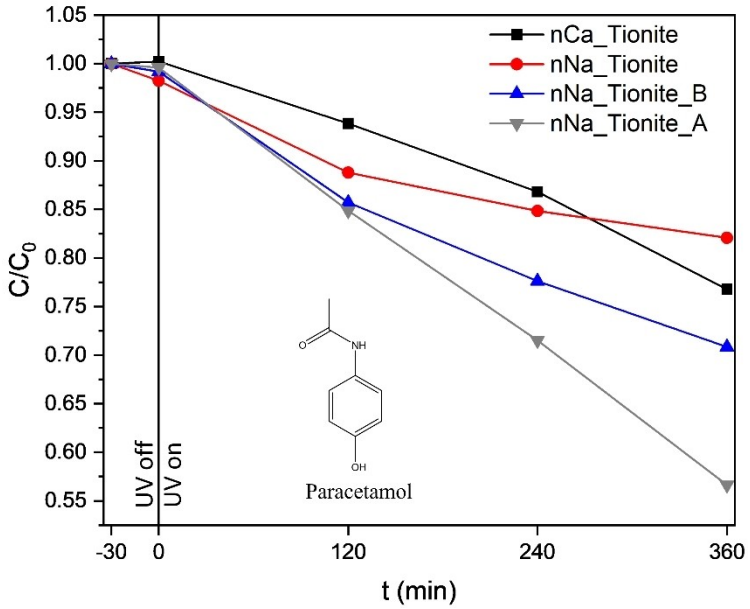

Figure 9. Variation of PC concentration by photo-degradation with nCa_Tionite (black), nNa_Tionite (red), nNa_Tionite_B (blue) and nNa_Tionite_A (grey).

The photocatalytic production of vanillin has been reported with selectivity values of ca. 2% in the presence of the benchmark photocatalyst TiO_2 P25 under UVA light irradiation.[44] Therefore, exceeding these values is relevant, due to the high commercial value of vanillin. Moreover, the use of a waste material such as tionite as the photocatalyst is a remarkable added value for this reaction. It is worth noticing that the selectivity to vanillin obtained through photocatalysis can be significantly increased by coupling the photocatalytic reactor with membrane separation units. The features and the synergistic effects of this virtuous example of process intensification have been widely discussed in previous reports.[45]

Figure 10a reports the concentration of ferulic acid in irradiated aqueous suspension of the different tionite samples. A steep decrease in ferulic acid concentration could be observed within the first hour of irradiation while, thereafter, the concentration decreased more slowly. In particular, after the first hour of irradiation, the concentration decreased with a similar slope in the presence of the two untreated (raw) samples and nNa_Tionite_B. On the other hand, faster ferulic acid degradation is apparent in the presence of nNa_Tionite_A sample, in agreement with what observed for the degradation of PC. The similar photoactivity of the nCa_Tionite, nNa_Tionite and nNa_Tionite_B samples is related to the similar surface properties of their photoactive TiO_2 component. On the other hand, the presence of fluoride groups at the surface of the nNa_Tionite_A sample increases the photocatalytic activity due to the often-reported beneficial effect of fluorination in terms of

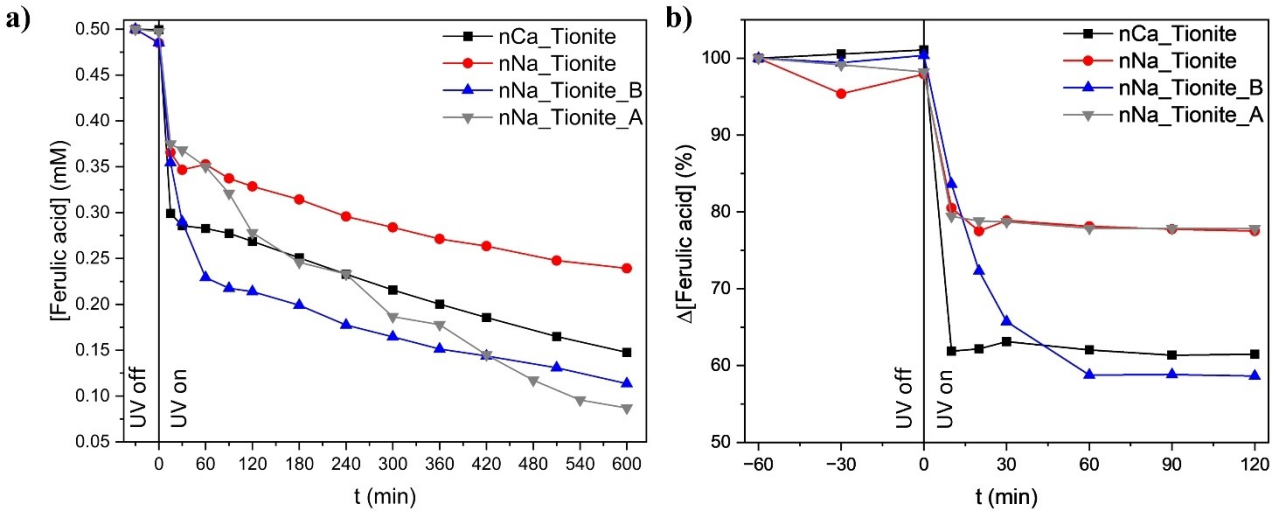

Figure 10. Variation of the ferulic acid concentration in oxygenated (a) or deaerated (b) suspensions of nCa_Tionite (black), nNa_Tionite (red), nNa_Tionite_B (blue) and nNa_Tionite_A (grey), under UVA light irradiation.

hydroxyl radicals generation.[46] In fact, surface fluorine groups, unlike hydroxyl ones, cannot act as surface hole traps being too high the oxidation potential of the $F^{\bullet}/F^{-}$ couple (3.6 V vs NHE), thus resulting in enhanced availability of holes for the direct water oxidation, which in turn results in higher production of hydroxyl radicals.[46]

In order to correctly interpret the steep decrease in the ferulic acid concentration observed in the first hour of irradiation, we performed the same reaction under continuous nitrogen bubbling, by keeping constant all of the other experimental conditions. Results are shown in Figure 10b. In the absence of oxygen, the ferulic acid concentration decreases at the beginning of the test similarly to what is observed in the oxygenated suspension but, thereafter, it remains constant. This result indicates that ferulic acid strongly adsorbs under irradiation onto all of the tionite samples, especially for nCa_Tionite and nNa_Tionite_B, whose surface, therefore, undergoes the most relevant changes when irradiated.[47] After reaching photo-stationary equilibrium (after the first hour), the ferulic acid concentration remained constant due to the prevailing recombination of the photogenerated charges, which occurs preferentially in the absence of suitable electron acceptor species. On the other hand, under dark conditions, the adsorption of ferulic acid onto all of the samples is negligible, as suggested by the concentration values measured prior to irradiation and as confirmed by systematic dark-adsorption experiments carried out independently (data not reported).

Concomitant vanillin production under irradiation in the oxygenated suspensions of all tionite samples was observed. Figure 11 reports the vanillin selectivity values calculated during irradiation according to Eq. 1, as reported in the Paragraph 2.4

According to Figure 11, all samples show a gradual increase in the S% values but two different trends can be highlighted: both nNa_Tionite and nNa_Tionite_A photocatalysts produce a similar and more rapid increase in the vanillin selectivity compared to nCa_Tionite and nNa_Tionite_B samples. Notably,

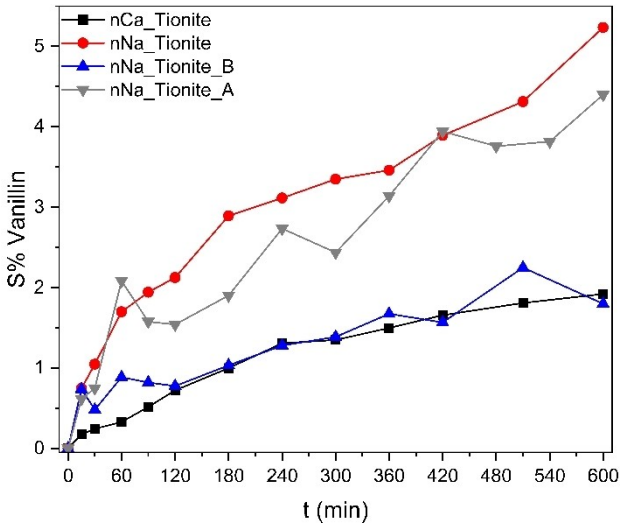

Figure 11. Selectivity towards vanillin as a function of the irradiation time in the presence of nCa_Tionite (black), nNa_Tionite (red), nNa_Tionite_B (blue) and nNa_Tionite_A (grey) samples.

under the same experimental conditions, P25 provided a maximum selectivity of only 2%.[44]

Comparing the results in Figures 9 and 10, it is evident a strong correlation between the photoadsorption behavior of the tionite samples and the selectivity towards vanillin obtained in the corresponding photocatalytic runs. In fact, the selectivity values towards vanillin obtained under irradiation follows almost linearly the photo-induced capability of the photocatalysts to adsorb organic species. This behavior confirms the hypothesis that the selectivity towards partial oxidation products is strictly related to their affinity with the surface.[48] In other words, the higher the affinity with the surface of the photocatalyst, the higher the probability that the intermediate compound of interest is overoxidized, thus dramatically reducing the selectivity of the reaction. However, this effect has been previously correlated with the adsorption behavior under dark conditions. Hereby, for the first time, the importance of surface phenomena in determining the selectivity of partial oxidation reactions can be assessed when irradiation dramatically changes the surface features of the photocatalyst, as in the case of tionite samples.

A relevant question, however, arises by considering that both nNa_Tionite and nNa_Tionite_B samples show dramatically different behavior under irradiation in terms of photoadsorption and selectivity to vanillin, even though they possess quite similar morphological and surface features, as highlighted by the characterization results. It is worth to remember here that the only relevant difference between the two samples relies in their composition. In fact, besides a photo-active TiO_2 portion of comparable features in the two photocatalysts, the nNa_Tionite sample is also composed of *ca.* 55% of an aluminosilicate component, which is not photoactive. The effects of "inert" components in tailored photocatalysts have been reported to be beneficial in addressing the selectivity of photocatalytic partial oxidation reactions, producing a specific product distribution deriving from different reactive oxygen species thereby generated.[49] However, unlike the mentioned literature studies, no different product distribution is observed in the present case. In order to highlight the reasons underlying the different behavior of nNa_Tionite and nNa_Tionite B samples we investigated the adsorption behavior of vanillin under dark in the presence of opportune amounts of the catalysts to keep constant the amount of the TiO_2 component (0.45 mg/ml). Therefore, results in Figure 12a express the absolute amount of vanillin adsorbed in the dark at equilibrium. For the sake of completeness, the corresponding plot obtained by considering the adsorption values per mass of the catalyst is reported in Figure S7, along with the calculated thermodynamic parameters.

The maximum amount of vanillin adsorbed at equilibrium in the dark is higher for the nNa_Tionite sample. By considering comparable the surface features of the TiO_2 component in the two samples, according to the characterization results, and considering that the amount of TiO_2 in the two samples is the same, this difference can be ascribed to the vanillin adsorption behavior of the aluminosilicate component present in the nNa_Tionite sample, which thus adsorbs similar amounts of vanillin

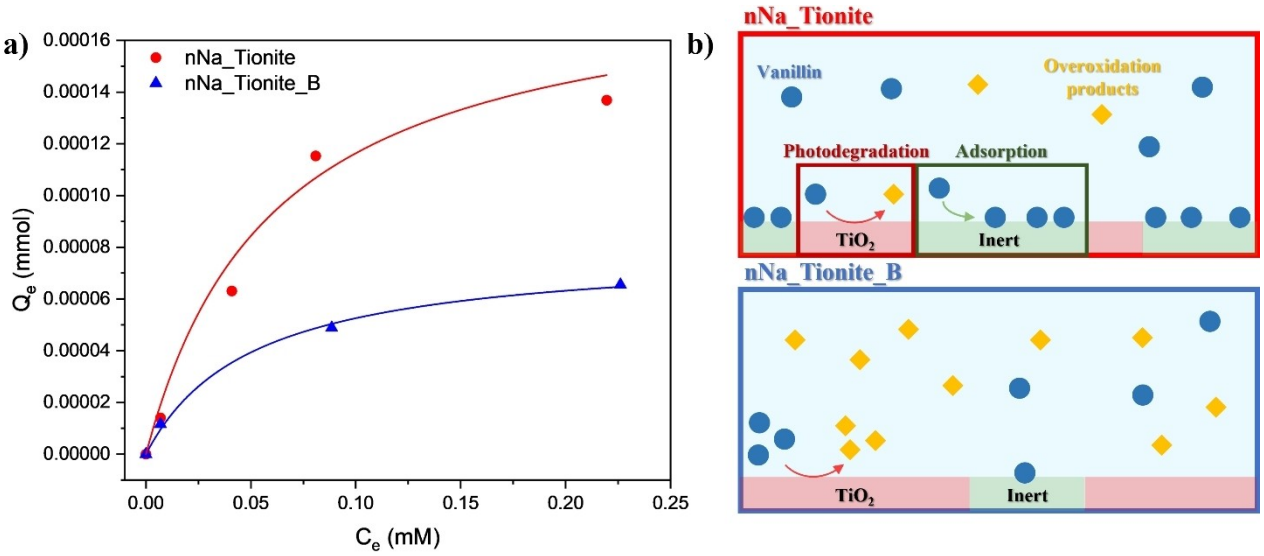

Figure 12. a) Langmuir fitting (solid lines) of the vanillin adsorption results and b) scheme of the photo-induced overoxidation reactions of vanillin at the surface of nNa_Tionite (red) and nNa_Tionite_B (blue) samples.

in the dark. In fact, the maximum amount of vanillin adsorbed by the nNa_Tionite sample (0.0187 mmol) is ca. 55% higher than the one adsorbed by nNa_Tionite_B sample (0.0102), which corresponds to the amount of aluminosilicate component (55%) present in the nNa_Tionite sample.

The ability of the aluminosilicate component to adsorb vanillin could justify the different selectivities obtained in the presence of irradiated nNa_Tionite and nNa_Tionite_B samples as schematically depicted in Figure 12b. In fact, the vanillin photocatalytically produced onto the TiO_2 component of the samples could easily undergo further oxidation in the nNa_Tionite_B sample, while the non-photo-active aluminosilicate component of the nNa_Tionite sample can adsorb vanillin by consequently preventing its photocatalytic decomposition. Similar hypothesis has been invoked by Tsukamoto et al.[50] for the partial oxidation of alcohols to aldehydes in the presence of TiO_2/WO_3 composites synthetized on purpose. The WO_3 component that is partially covering TiO_2, was not able to over-oxidize the aldehyde products, thus resulting in higher selectivity values. The peculiar interaction between photo-active and non photo-active components intrinsically present in the waste material tionite, is a useful feature for photocatalytic partial oxidations and could be used for further similar applications.

4. Conclusions

A tailored regeneration strategy was for the first time successfully implemented to enable the reuse of tionite, a waste material obtained from TiO_2 industrial production. The chemical treatments applied were selected in order to purify the waste and to increase the accessibility of titanium dioxide, in view of possible photocatalytic applications. Preliminary results on PC photocatalytic degradation showed low activity of the modified tionite materials, and encouraged us in exploring possible applications in the field of partial oxidation reactions. The photocatalytic conversion of ferulic acid to vanillin was chosen as a model reaction, considering the remarkable features of this process in terms of sustainability and economic impact. All of the tionite-based catalysts have shown a gradual increase of the vanillin selectivity under irradiation, with the better perfomances obtained in the presence of nNa_Tionite_A sample. This was attributed to the positive effects of fluorination in terms of hydroxyl radical production and to the limited vanillin adsorption on the catalyst surface, which limited its overoxidation.

Declaration of Competing Interest

The authors declare that they have no known competing financial interests or personal relationships that could have appeared to influence the work reported in this paper.

Acknowledgments

BDC thanks Prof. Giuliana Magnacca of the University of Turin for her contribution to BET analysis. Open Access publishing facilitated by Università degli Studi di Milano-Bicocca, as part of the Wiley - CRUI-CARE agreement. Open Access publishing facilitated by Università degli Studi di Milano-Bicocca, as part of the Wiley - CRUI-CARE agreement.

Conflict of Interests

The authors declare no conflict of interest.

Data Availability Statement

The data that support the findings of this study are available in the supplementary material of this article.

Keywords: Tionite · Titanium dioxide · Recovery · Photocatalysis · Vanillin

[1] World Economic Forum. *The Global Risks Report - 19th Edition*, **2024**.
[2] United Nations Environment Assembly - 2nd session, *Res UNEP/EA.2/Res.7*, **2016**.
[3] S. Latorrata, R. Balzarotti, M. I. Adami, B. Marino, S. Mostoni, R. Scotti, M. Bellotto, C. Cristiani, *Appl. Sci.* **2021**, *11*, 2985.
[4] J. D. Kabongo, *Waste Valorization*, Springer Berlin Heidelberg, Berlin, Heidelberg, **2013**
[5] F. Meng, T. Xue, Y. Liu, W. Wang, T. Qi, *Hydrometallurgy* **2016**, *161*, 112–116.
[6] M. D'Arienzo, M. V. Dozzi, M. Redaelli, B. Di Credico, F. Morazzoni, R. Scotti, S. Polizzi, *J. Phys. Chem. C* **2015**, *119*, 12385–12393.
[7] F. Gherardi, A. Colombo, M. D'Arienzo, B. Di Credico, S. Goidanich, F. Morazzoni, R. Simonutti, L. Toniolo, *Microchem. J.* **2016**, *126*, 54–62.
[8] B. Di Credico, M. Redaelli, M. Bellardita, M. Calamante, C. Cepek, E. Cobani, M. D'arienzo, C. Evangelisti, M. Marelli, M. Moret, L. Palmisano, R. Scotti, *Catalysts* **2018**, *8*, 3532.
[9] P. Blanchart, Extraction, Properties and Applications of Titania. In *Industrial Chemistry of Oxides for Emerging Applications* P. John Wiley & Sons, LTD, Hoboken, NJ, USA, **2018**, 255-309.
[10] F. Parrino, L. Palmisano, *Titanium Dioxide (TiO_2) and Its Applications*, Elsevier, Amsterdam, The Netherlands, **2021**.
[11] A. H. J. Sampath, N. D. Wickramasinghe, K. M. N. de Silva, R. M. de Silva, *Minerals* **2023**, *13*.
[12] C. Thambiliyagodage, R. Wijesekera, M. G. Bakker, *Discov. Mater.* **2021**, *1*, 20 .
[13] M. J. Gázquez, J. Mantero, J. P. Bolívar, R. García-Tenorio, F. Vaca, R. L. Lozano, *J. Hazard. Mater.* **2011**, *191*, 269–276.
[14] W. Hajjaji, G. Costa, C. Zanelli, M. J. Ribeiro, M. P. Seabra, M. Dondi, J. A. Labrincha, *J. Eur. Ceram. Soc.* **2012**, *32*, 753–764.
[15] J. A. Labrincha, J. I. Marques, W. Hajjaji, L. Senff, C. Zanelli, M. Dondi, F. Rocha, *Waste Biomass Valorization* **2014**, *5*, 385–392.
[16] W. Hajjaji, C. Zanelli, M. P. Seabra, M. Dondi, J. A. Labrincha, *Chem. Eng. J.* **2011**, *171*, 1178–1184.
[17] S. M. Pérez-Moreno, M. J. Gázquez, A. G. Barneto, J. P. Bolívar, *Thermochim. Acta* **2013**, *552*, 114–122.
[18] A. Basso Peressut, C. Cristiani, G. Dotelli, A. Dotti, S. Latorrata, A. Bahamonde, A. Gascó, D. Hermosilla, R. Balzarotti, *Nanomaterials* **2023**, *13*, 1043.
[19] R. Delisi, R. Ciriminna, F. Parrino, L. Palmisano, Y.-J. Xu, M. Pagliaro, *ChemistrySelect* **2016**, *1*, 626–629.
[20] R. Ciriminna, R. Delisi, F. Parrino, L. Palmisano, M. Pagliaro, *Chem. Commun.* **2017**, *53*, 7521–7524.
[21] J.-P. Vidal. Vanillin. In *Kirk-Othmer Encyclopedia of Chemical Technology*, John Wiley & Sons, LTD, Hoboken, NJ, USA, **2006**.
[22] M. Dondi, G. Guarini, M. Raimondo, C. Zanelli, D. D. Fabbriche, A. Agostini, *Ceram. Int.* **2010**, *36*, 2461–2467.
[23] S. Brunauer, P. H. Emmett, E. Teller, *J. Am.Chem.Soc.* **1938**, *60*, 309–319.
[24] I. Langmuir, *J. Am. Chem. Soc.* **1918**, *40*, 1361–1403.
[25] S. Challagulla, K. Tarafder, R. Ganesan, S. Roy, *Sci. Rep.* **2017**, *7*, 8783–.
[26] F. C. Donnelly, F. Purcell-Milton, V. Framont, O. Cleary, P. W. Dunne, Y. K. Gun'ko, *Chem. Commun.* **2017**, *53*, 6657–6660.
[27] N. Krishnamurthy, V. Soots, *Can. J. Phys.* **1971**, *49*, 885–896.
[28] Y. Liu, A. Wang, J. J. Freeman, *40th Lunar and Planetary Science Conference* 2009, 2128.
[29] Y. Ennaciri, H. El Alaoui-Belghiti, M. Bettach, *J. Mater. Res. Technol.* **2019**, *8*, 2586–2596.
[30] P. Praveen, G. Viruthagiri, S. Mugundan, N. Shanmugam, *Spectrochim. Acta - Part A Mol. Biomol. Spectrosc.* **2014**, *117*, 622–629.
[31] F. Paulik, J. Paulik, M. Arnold, *Thermochim. Acta* **1992**, *200*, 195–204.
[32] T. Siva, S. Muralidharan, S. Sathiyanarayanan, E. Manikandan, M. Jayachandran, *J. Inorg. Organomet. Polym. Mater.* **2017**, *27*, 770–778.
[33] M. H. H. Mahmoud, M. M. Rashad, I. A. Ibrahim, E. A. Abdel-Aal, *J. Colloid Interface Sci.* **2004**, *270*, 99–105.
[34] S. Liu, J. Yu, B. Cheng, M. Jaroniec, *Adv. Colloid Interface Sci.* **2012**, *173*, 35–53.
[35] Z. Shayegan, F. Haghighat, C. S. Lee, A. Bahloul, M. Huard, *Chem. Eng. J.* **2018**, *346*, 578–589.
[36] N. Fessi, M. F. Nsib, Y. Chevalier, C. Guillard, F. Dappozze, A. Houas, L. Palmisano, F. Parrino, *Langmuir* **2020**, *36*, 13545–13554.
[37] N. Fessi, M. F. Nsib, L. Cardenas, C. Guillard, F. Dappozze, A. Houas, F. Parrino, L. Palmisano, G. Ledoux, D. Amans, Y. Chevalier, *J. Phys. Chem. C* **2020**, *124*, 11456–11468.
[38] M. Thommes, K. Kaneko, A. V. Neimark, J. P. Olivier, F. Rodriguez-Reinoso, J. Rouquerol, K. S. W. Sing, *Pure Appl. Chem.* **2015**, *87*, 1051–1069.
[39] M. Thommes, B. Smarsly, M. Groenewolt, P. I. Ravikovitch, A. V. Neimark, *Langmuir* **2006**, *22*, 756–764.
[40] J. Yu, W. Wang, B. Cheng, B. L. Su, *J. Phys. Chem. C* **2009**, *113*, 6743–6750.
[41] Y. S. Lee, Y. H. Kim, J. S. Hong, J. K. Suh, G. J. Cho, *Catal. Today* **2007**, *120*, 420–425.
[42] W. Koagouw, N. A. Stewart, C. Ciocan, *Environ. Sci. Pollut. Res.* **2021**, *28*, 48823–48836.
[43] N. Blangetti, F. S. Freyria, M. C. Calviello, N. Ditaranto, S. Guastella, B. Bonelli, *Catalysts* **2023**, *13*, 434 .
[44] V. Augugliaro, G. Camera-Roda, V. Loddo, G. Palmisano, L. Palmisano, F. Parrino, M. A. Puma, *Appl. Catal. B Environ.* **2012**, *111–112*, 555–561.
[45] M. Bellardita, G. Camera-Roda, V. Loddo, F. Parrino, L. Palmisano, *Catal. Today* **2020**, *340*, 128–144.
[46] M. Mrowetz, E. Selli, *Phys. Chem. Chem. Phys.* **2005**, *7*, 1100–1102.
[47] F. Parrino, V. Loddo, V. Augugliaro, G. Camera-Roda, G. Palmisano, L. Palmisano, S. Yurdakal, *Catal. Rev. - Sci. Eng.* **2019**, *61*, 163–213.
[48] F. Parrino, C. De Pasquale, L. Palmisano, *ChemSusChem* **2019**, *12*, 589–602.
[49] A. Gottuso, A. Köckritz, M. L. Saladino, F. Armetta, C. De Pasquale, G. Nasillo, F. Parrino, *J. Catal.* **2020**, *391*, 202–211.
[50] D. Tsukamoto, M. Ikeda, Y. Shiraishi, T. Hara, N. Ichikuni, S. Tanaka, T. Hirai, *Chem. – A Eur. J.* **2011**, *17*, 9816–9824.

Manuscript received: July 31, 2024
Revised manuscript received: October 14, 2024
Accepted manuscript online: October 15, 2024
Version of record online: ■■, ■■